Polymer 107 (2016) 89–101

Contents lists available at ScienceDirect

Polymer

journal homepage: www.elsevier.com/locate/polymer

Multiscale organization of thermoplastic elastomers with varying content of hard segments

Guilhem P. Baeza [a, *], Ashwinikumar Sharma [b, c], Ameur Louhichi [a, d], Luna Imperiali [c], Wilco P.J. Appel [c], Carel F.C. Fitié [c], Minne P. Lettinga [e], Evelyne Van Ruymbeke [b], Dimitris Vlassopoulos [a, d]

[a] Foundation for Research and Technology – Hellas (FO.R.T.H), Institute of Electronic Structure and Laser, N. Plastira 100 - Vassilika Vouton, Heraklion, Crete, 70013, Greece
[b] Bio and Soft Matter, Institute on Condensed Matter and Nano-science, Université catholique de Louvain, Louvain-la-Neuve, Belgium
[c] DSM Ahead (DSM Engineering Plastics), Urmonderbaan 22, 6167RD, Geleen, The Netherlands
[d] Department of Materials Science and Technology, University of Crete, P.O. Box 2208, 71003, Heraklion, Greece
[e] Forschungszentrum Jülich, Institute of Complex Systems (ICS-3), 52425, Jülich, Germany

ARTICLE INFO

Article history:
Received 5 October 2016
Received in revised form
4 November 2016
Accepted 6 November 2016
Available online 8 November 2016

Keywords:
Thermoplastic elastomers
H-bonds
Scattering

ABSTRACT

Thermoplastic elastomers (TPEs) based on segmented block-copolymers containing poly(-tetrahydrofuran) (pTHF) and terephthalate-based diamide groups (T4T) were synthesized via poly-condensation. While pTHF is known to be flexible and amorphous at rest, the more rigid T4T crystallized in different ways depending on both chain composition and sample preparation conditions. Increasing the content of hard-segments (HS) from 5 to 20% in weight leads to a substantial increase of the melting point T_m by more than 60 °C. We have systematically investigated the multiscale (1 Å - 50 nm) organization of the HSs (of fractions from 5% to 20%) by means of DSC, WAXS and (ultra) small angle X-ray scattering (U)SAXS. By increasing HS content, hence the rigidity of the chain, scattering experiments unambiguously show the formation of bigger and better defined ribbon-like crystallites, as well as the densification of the network they form. We propose a scenario for rationalizing the local T4T-HSs packing and the crystallites anisotropy at the mesoscale (1–10 nm) for HS fraction above 5%. Moreover, following in-situ the crystallization of TPEs with large HS fraction (20%), we highlight the presence of "persistent aggregates" present at $T > T_m$ and study the ribbon-like crystallites growth mechanism during cooling from the melt state.

1. Introduction

The name "thermoplastic elastomer" (TPE) refers to polymeric materials exhibiting a dual rubber/melt rheological behavior as opposed to classic vulcanized rubbers [1,2]. Their high elasticity and flexibility at operating temperature (−50 to 50 °C) reflects thermo-reversible phase separation [1], which gives rise to rubber-like properties without involving chemical crosslinks. This reversibility makes the TPEs good candidates for a more sustainable rubber production (recycling of vulcanized rubber is difficult and marginal [2]), in particular in terms of reshaping and recycling many daily consumer goods. Since the 1960's, a wide variety of industrial relevant TPEs have been synthesized [3]. One of the most popular examples is the PS-PB-PS tri-block copolymer [4] where the segregation of the PS blocks forming rigid subdomains confers rubber-like mechanical properties to the material. While the general phase separation mechanism of these systems is understood, it stays crucial for the industry to be able to control and tailor their properties in order to use them in many different applications. This requires being able to control the transition from their melt to their gel state (and vice versa) in terms of both temperature and mechanical properties. In this direction, rather than letting the (in) compatibility of the two blocks controlling phase separation kinetics and final morphology [5], researchers have developed new generations of TPEs based on supramolecular interactions, which involve new parameters to tailor the properties of such materials. One of the most popular approaches is the synthesis of segmented

* Corresponding author. Current address: MATEIS, INSA-Lyon, CNRS UMR5510, F-69621, Lyon, France.
E-mail address: guilhem.baeza@insa-lyon.fr (G.P. Baeza).

http://dx.doi.org/10.1016/j.polymer.2016.11.010
0032-3861/

(or multi-block) copolymers with flexible units made of poly(-tetrahydrofuran) (pTHF) (also called poly-tetramethylene oxide, pTMO) linear motifs (soft-segments "SS") and rigid units (hard-segments "HS") based on urea [6], urethanes [7] or amide groups, as thoroughly studied by Gaymans [8]. The latter segmented copolymers are of particular interest due to their ability to generate multiple hydrogen bonds through the amide (i.e. N–H vs. C=O) groups, enhancing the aggregation and/or crystallization of the rigid segments in a similar way as in the well-known polyamides PA6 and PA66 *Nylons* [9]. In this context, several studies have shown the importance of monodisperse HSs which crystallize [8,10] by forming a regular ribbon-like structure (elongated soft objects), providing to the material tunable rheological properties as well as enhanced thermal and chemical stability. Monodisperse HSs also ensure a very fast crystallization upon cooling and a high melting temperature. Furthermore, using short and monodisperse hard segments allows reducing liquid-liquid demixing of the hard and soft segments when reducing temperature, while keeping a high rate of crystallization [11].

So far, a lot of effort has been put on the description of the thermomechanical properties [12], the identification of the crystalline phases [13] as well as the synthesis of new SS/HS motifs [14] with the key result being the systematic raise of both melting point and plateau modulus with increasing the HS content. However, many questions remain about the structure at the mesoscale level (5–100 nm) of the crystalline hard phase, which is a difficult task for semi-crystalline polymers. Nevertheless, this is of central importance for understanding their mechanical and viscoelastic behavior. The most frequently used techniques for determining the structure of such TPEs at the mesoscale level are atomic force microscopy (AFM) [15] and transmission electronic microscopy (TEM) [16] applied on solvent casted films. However, while they reveal interesting structures [6b,16-17], one needs to account for the fact that the observed organization strongly depends on the protocol used to prepare the sample. Indeed, structure in solvent casted films significantly differs from the one of the samples processed by extrusion from the melt state (without solvent), i.e. the ones of interest for studying viscoelastic and mechanical properties as well as for developing possible applications (3D printing, fibers production …). The latter, in fact, seem to be characterized by a more complex organization, in which the crystallites are likely more polydisperse and less aligned, hardly accessible with those techniques [6a].

Small Angle X-ray (or Neutron) Scattering (SAX(N)S) is widely employed [18] but often limited to the observation of the inter-crystallite distance [17] except for the extensive and inspiring work by Sijbrandi et al. [13] which provides a quantitative analysis of the crystal lattice as well as the mesoscale (hexagonal) structure of polyamide based ribbon crystallites. Moreover, the scattering cross section per unit sample volume, or "scattering intensity" $I(q)$, is almost exclusively expressed in arbitrary units (rather than absolute units) limiting *de facto* the structural analysis to the extraction of typical distances in the materials (along the q axis), i.e. ignoring the mass of the scattering objects required to establish a coherent model. Then, because of the very short (yet monodisperse) length of HSs, one cannot use the available molecular theory for similar block-copolymers [19] where phase segregation appears at high values of the Flory-Huggins parameter $(N\chi) \approx (N\chi)_c$ (where $(N\chi)_c$ is the critical value for spinodal decomposition with N the degree of polymerization). Indeed, it does not seem suitable for quick crystallization processes generating phase separation on a micrometer scale.

Going further in the employment of SAXS, one could model ribbon-like objects by using the form factor of semi-flexible chains with self-avoidance calculated by Pedersen et al. [20] This method, which has been successfully used by Hamley et al. [21] for worm-like micelles having a fractal dimension of $D_f \approx 1.7$, allowed the authors to determine directly the contour length, the persistence length and the cross-sectional radius of such elongated structure. However, this model lies on the fact that such objects do not interact with each other, i.e. that their volume fraction must be kept smaller than 1 vol%, far from the type of samples investigated in this work (ca. 5 to 20%v).

Thus, despite the above developments, many questions still need to be addressed in order to understand and control the structure of these TPEs, processed in the melt state. They concern, in particular, (i) the local packing of the T4T units leading to polymorphic crystals, (ii) the crystallites shape and their orientation at the mesoscale being of great interest for the rheology comprehension and (iii) the growth mechanism from the initial state (melt or in solvent). In this context, the key goal is to develop criteria for designing TPE materials with desired performances easily processable at the industrial scale.

The objective of the present work is to combine DSC, WAXS and (U)SAXS techniques in order to investigate the multiscale structure of segmented copolymers with a monodisperse hard-segment made of T4T diamide consisting mainly in two terephthalate "T" groups separated by four "4" carbon atoms [22]. (Other "T-amides" groups are reported in the literature) [23]. In particular, we would like to study the influence of the HS density on the crystallization and melting of such TPEs. The HS is characterized by a high melting (or crystallization) temperature, e.g., close to $T_m = 158$ °C (or $T_c = 136$ °C) [24] for 20%HS in the chains. On the other side, the SS is made of a sequence of 3 and 8.6 pTHF motifs (respectively called $pTHF_{250}$ and $pTHF_{650}$) between which a terephthalate group is intercalated to limit their crystallization (see Fig. 1). Based on these two elementary building blocks, we prepared four different copolymers (following a Flory-type statistic) by adjusting the HS nominal mass fraction to 5, 10, 15 and 20%. The average molar mass of the SSs is varied from 6840 g/mol (5%HS) to 3299 g/mol, (10%HS), 2078 g/mol (15%HS) and 1470 g/mol (20%HS) so that the total molecular weight of the four TPEs remain comparable (see Table 1).

The outline of this article is as follows. After the materials and methods description in section 2, the results are presented and discussed in section 3. DSC thermograms of the four TPEs and the neat pTHF are provided in section 3.1. The analysis of the crystal lattice using WAXS is presented in section 3.2, where new arguments to rationalize the T4T diffractograms are provided. Finally, section 3.3 is devoted to the (U)SAXS experiments in which we propose a method to determine the "micro-" (<10 nm) and "meso-" (10–50 nm) scale structure of the ribbons-like crystallites. In this last part, we also propose a growth mechanism based on time resolved SAXS measurements performed between T_m and T_c.

2. Material and methods

2.1. Materials

1,4-Diaminobutane (DAB), acetone and acetonitrile were obtained from Sigma Aldrich, USA, Dioctyl terephthalate (DOT) from Eastman chemicals, pTHF (650 g/mol and 250 g/mol) from BASF chemicals, Irganox 1330 from Ciba, Switzerland. Sodium ethoxide (21 wt% in ethanol) with Acroseal© from Acros, Belgium. All chemicals were used as received. Sodium ethoxide 21 wt% in ethanol was used to prepare sodium ethyl hexoxide 1 molar solution by replacing ethanol by ethyl hexanol using a distillation setup.

2.2. Synthesis T4T-dioctyl

DAB (30 g, 0.34 mol) and DOT (574 g, 1.46 mol) were introduced

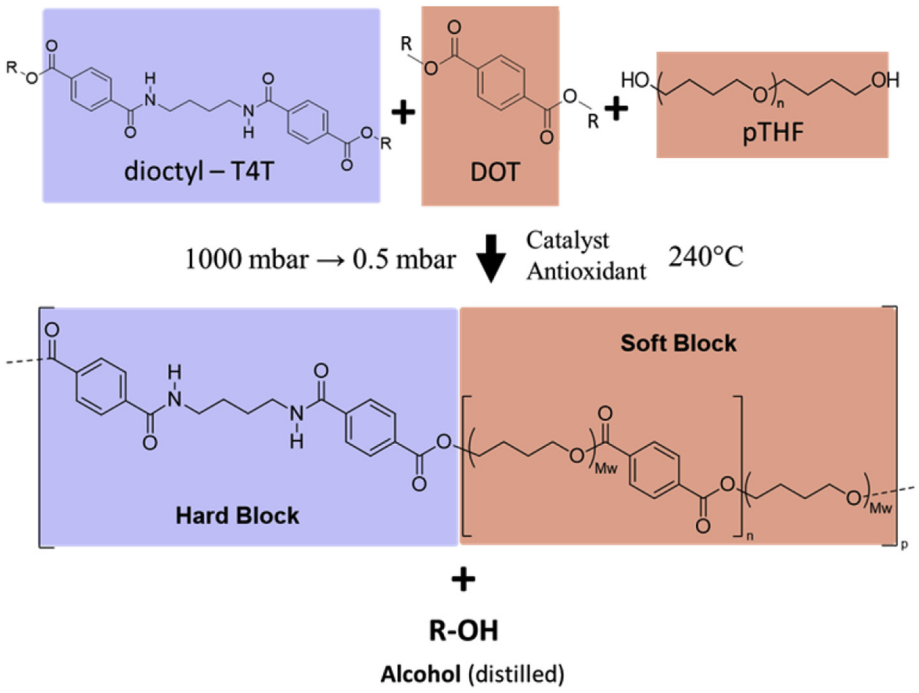

Fig. 1. Schematic of the pTHF-T4T segmented block copolymers. **R** stands for an Octyl group, and DOT for dioctyl-Terephtalate.

Table 1
Physico-chemical characterization related with the TPEs studied.

%HS (%)	M_n (g/mol)	M_w (g/mol)	M_w/M_n (Ø)	M_n(pTHF)[a] (g/mol)	<N>[b] (Ø)	T_g^{SS} (°C)	T_m (°C)	T_c (°C)	X_c[c] (%)
5	25,200	48,900	2	6840	4	−59.1	91.8	64.5	2.6
10	22,800	44,300	2	3299	7	−58.8	122.3	100.1	6.3
15	22,500	43,300	2	2078	11	−57.9	148.6	119.8	9.3
20	19,300	37,600	2	1470	11	−57.9	157.8	136.4	15.8

[a] Average molar mass of the pTHF segments between two successive HS as calculated based on the synthesis.
[b] Average number of HS per chain calculated from %HS and M_n.
[c] Crystal weight fraction from DSC calculated via $X_c = (\Delta H_{DSC}/\Delta H_{T4T})^*100$ where $\Delta H_{T4T} = 150$ J g^{-1} from Ref. [25].

in a round bottom flask equipped with stirrer and nitrogen inlet. Then, 61 cm^3 Sodium ethyl hexoxide solution (1 M) was added and the reaction was carried out for 24 h at room temperature under a nitrogen atmosphere. It was subsequently quenched using 10 cm [3] water. The T4T-dioctyl was precipitated and filtered using 2 liters of acetone. The crude T4T-dioctyl was recrystallized from hot acetonitrile and washed with acetonitrile thrice. The purified T4T-dioctyl was finally dried overnight in a vacuum oven at 65 °C. The corresponding DSC and NMR measurements are provided respectively in Figs. S1 and S2 of supplementary information.

2.3. Melt polycondensation of 5 wt% T4T-($PTMO_{650}$/DOT/$PTMO_{250}$)

The reaction was carried out in a glass vessel reactor with nitrogen inlet, distillation set-up and mechanical stirrer. The reactor was loaded with T4T-dioctyl (8.31 g, 0.0136 mol), $pTHF_{650}$ (57.22 g, 0.880 mol), $pTHF_{250}$ (22.04 g, 0.0220 mol), DOT (57.19 g, 0.05719 mol), Irganox 1330 antioxidant (0.25 g, 0.0003 mol) and Titanium catalyst (0.57 g, 0.0037 mol) and heated to 240 °C under a reduced pressure of 500 mbar. Subsequently, the pressure was decreased to 10 mbar over a period of 2.5 h. With increasing the viscosity of the melt, the stirring rate was gradually reduced from 400 rpm to 100 rpm. The pressure was further reduced to 1 mbar in 3 h and subsequently kept constant for 3 h while gradually reducing the stirring rate to 12 rpm. The polymer was then removed from the reactor, quenched in water and finally dried overnight in a vacuum oven at 65 °C. A similar procedure was used for 10 wt%, 15 wt% and 20 wt% hard-segment (T4T) copolymer synthesis by adjusting the amounts of the ingredients accordingly. The schematic procedure is depicted in Fig. 1.

2.4. Gel permeation chromatography

Gel permeation chromatography was performed on the full sample set with a Viscotek GPC Max from Malvern (UK) equipped with a Viscotek Triple Detector Array 302 including ultra-violet (UV), refractive index (RI), differential viscometer (DV) and right-angle light-scattering (RALS) detector so no column calibration was necessary. The TPEs were dissolved in HFIP at a concentration of 1.5 mg/mL, filtered with 0.2 μm Teflon filters, and injected at a rate of 0.8 mL/min. The temperature of both the column and the detector was kept constant at 35 °C. The results in terms of M_n and M_w are presented in Table 1.

2.5. Samples preparation

The samples measured in DSC, WAXS and (U)SAXS were prepared either by hot pressing or solvent casting. In the former case,

ca. 0.5 g of TPE was molten in a vacuum hot press at T_m + 10 °C applying 0.5 tons weight for 30 min and subsequently quenched in ice. In the latter case, the TPE was dissolved for 12 h in TetraHydroFuran (THF) or HexaFluoroIsoPropanol (HFIP) and subsequently dried by evaporating the solvent at room temperature for 48 h before to be dried one week under vacuum at room temperature.

2.6. Differential scanning calorimetry (DSC)

DSC thermograms for polymers were recorded on a Mettler Toledo DSC821e with the STARe software using dried samples of 10–14 mg with a heating and cooling rate of 20 °C/min. The peak positions of the second heating and first cooling scans were assigned to the transition temperatures T_m and T_c, respectively, and the area under the heating curve to the melting enthalpy ΔH_m. From the latter and the melting enthalpy of the T4T unit [25], the degree of crystallinity was then calculated (see Table 1). Note that the thermograms presented in Fig. 2 have been corrected in order to have a flat baseline.

2.7. WAXS

Wide Angle X-ray Scattering experiments were performed on a Rigaku DMAX 12 kW setup with λ = 1.54 Å. The beam size was 1 cm × 1 mm. We limited the angle range from 2θ = 1.5°–35° (corresponding to q = 1 nm^{-1} to 25 nm^{-1}) where the signature of all the crystalline phases and the amorphous broad peak were observable.

2.8. USAXS and SAXS

We performed USAXS and SAXS measurements on the beam line ID02 at the ESRF in Grenoble, France. The four samples made of segmented block copolymers containing 5, 10, 15 and 20%HS have been measured. Their respective thicknesses were 0.44, 0.81, 0.66 and 1.03 mm. We used two sample-detector distances, 1 m (SAXS) and 30 m (USAXS) with λ = 1.1 Å allowing to obtain information over 4 decades in scattering vector $\vec{q}$ (10^{-3} to 10 nm^{-1}) corresponding roughly in the real space to 1 μm to 1 Å. The beam was rectangular with an approximate size of 0.1 × 0.2 mm^2. The well-defined configuration of this experiment, associated with the measurement of the empty beam gave us the possibility to access the true sample scattering in absolute units.

In order to complement this data, we also performed SAXS measurements with temperature control on the beam line DUBBLE at the ESRF by using a Haake rheometer equipped with Vespel® parallel plates (no solicitation was applied). The incident horizontal X-ray beam was 90° deviated in order to pass vertically through the rheometer cell (two Vespel plates + sample) and the emerging scattering intensity was measured from the top of the setup, as in Ref. [26] For the detection of anisotropic scattering patterns, the novel LAMBDA detector, a 2D photon counting detector, developed at DESY, Hamburg, Pennicard et al. [27] was used. The LAMBDA has a high spatial resolution with a pixel size of 55 × 55 μm^2, a high quantum efficiency close to 100%, and a high speed acquisition of up to 2000 frames/sec [27] at 1.6 m from the sample and using a wavelength of 1.53 Å. Note that the data measured from DUBBLE were then rescaled to the ID02 ones in order to access the absolute units (see the procedure in Fig. S6 of supplementary information).

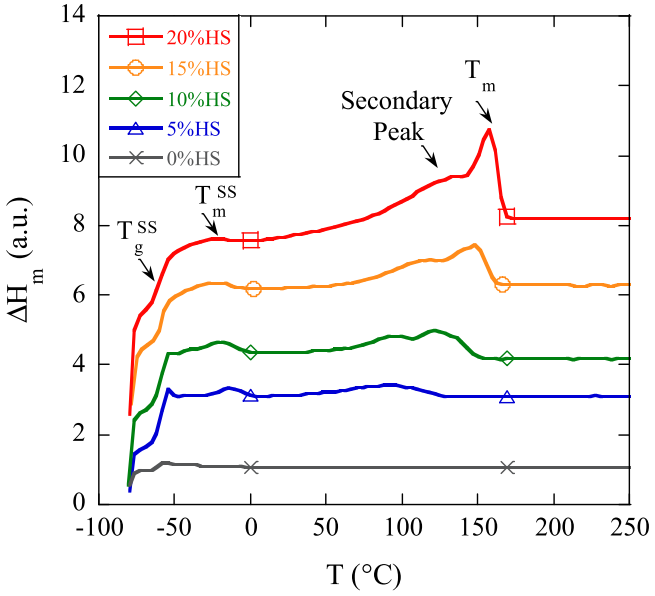

Fig. 2. Differential Scanning Calorimetry thermograms of the neat pTHF (0%HS) and the four corresponding segmented block copolymers containing 5, 10, 15 and 20%HS. The different T_g^{SS}, T_c (not shown here) and T_m are reported in Table 1. Data have been vertically shifted for clarity.

3. Results and discussion

3.1. Calorimetry

In Fig. 2 we present the thermograms corresponding to the four hot-pressed TPEs containing 5, 10, 15 and 20%HS for which the baseline has been forced to be horizontal (see. section 2). On one hand, the lowest temperature part of the thermograms remains essentially identical showing the glass transition of the pTHF at −60 °C (T_g^{SS}) and the melting of a small fraction of it close to −15 °C (T_m^{SS}). One can note, here, the slight increase of this peak with decreasing %HS likely due to larger pTHF domains [25]. On the other hand, the highest temperature part reveals a clear increase of the HS crystallites "terminal" melting point T_m from 91.8 to 122.3, 148.6 and 157.8 °C for 5, 10, 15 and 20%HS, respectively (see Table 1).

Moreover, the thermograms contain "secondary" melting peaks at $T \approx T_m$-30 °C, which are clearly visible for 10, 15 and 20%HS, suggesting a polymorphism of the T4T crystallites in agreement with the complex diffractograms presented in Fig. 3a below. From the broadening of this secondary peak at lower temperature with increasing %HS, one could also speculate on the presence of the glass transition temperature of a small fraction of residual amorphous T4T domains [28] (particularly for 20%HS around 20 °C), satisfying the well-known ratio $T_g/T_m \approx 2/3$ [29]. This would thus suggest that the HS crystallization is not fully complete for these samples, in agreement with the enthalpy of melting (~area under the curve) from which the degree of crystallinity can be extracted (see X_c Table 1).

Interestingly, one can also observe in Fig. 2 that increasing the HS density causes the shift of the "secondary" broad melting peak toward higher temperature in a similar way than the sharper one suggesting therefore that both melting processes are interdependent.

3.2. Crystal structure – WAXS

3.2.1. Analysis of scattering intensity and the role of hard segments

As it has been already observed in literature, the WAXS pattern related with the T4T crystal is rather complex and has not been elucidated so far [25]. In order to gain further insight, we compare it here to different samples, such as the pure HS sample or a solvent

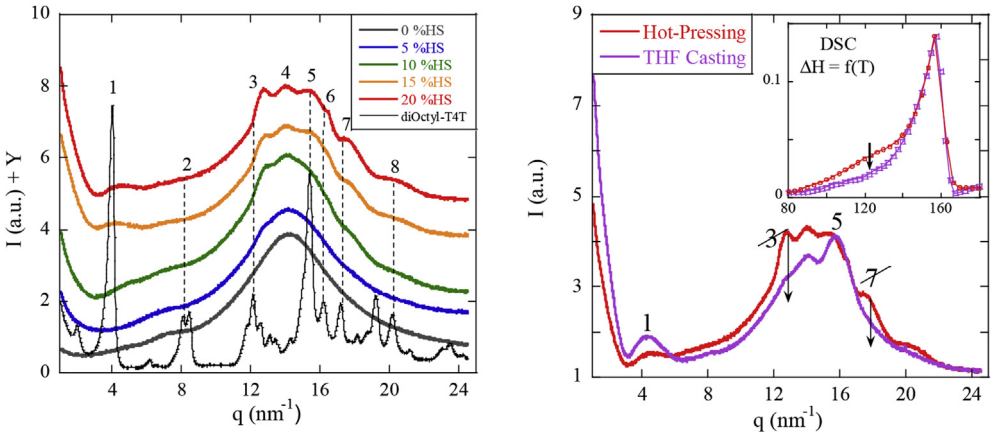

Fig. 3. a) Scattering intensity measured in WAXS as a function of the transfer momentum q for pure pTHF chains and dioctyl-T4T powder as well as for the four segmented block copolymers prepared by hot-pressing containing 5, 10, 15 and 20%HS. b) Diffractogram from the 20%HS sample prepared by solvent casting vs. the hot-pressed one reproduced from a). The data are normalized in such a way that the intensity of the peak 5 match. **Inset**: corresponding DSC thermograms in the T_m region confirming the weakening of the secondary melting peak when THF-casting is used.

casted version, and follow the relative intensities of the different peaks. In Fig. 3a, we present the diffractograms measured from the materials synthesized in this work (see section 2) from $q = 1$ to 25 nm^{-1} (i.e. $2\theta = 1.6–35°$). The main peaks observed through the whole data set are numbered from 1 to 8 from lower to higher q and reported in Table 2.

While these peaks are nearly absent in the sample containing 5% HS, their respective intensities increase with the fraction of hard segments, indicating unambiguously that they are coming from the crystallization of the HSs. Furthermore, a good agreement is found between the positions of most of the peaks in the TPEs chains and the ones coming from the dioctyl-T4T precursor, suggesting that the HS crystal lattice is qualitatively similar in all these materials when hot-pressing at $T_m + 10$ °C is used. The broad peak (4), present in all TPEs (including 0%HS) at 14 nm^{-1} is attributed to the amorphous part of the polymers and tell us about the typical distance between the pTHF segments ($\approx$0.45 nm). Overall, the WAXS patterns look similar to the one obtained by van Hutten et al. on similar materials [25].

Also, we observe in Fig. 3b, that the WAXS pattern of the 20%HS sample is very sensitive to the sample preparation. Indeed, the comparison between the normalized WAXS signals of sample prepared in the melt state or by solvent casting reveals that 20%HS sample exhibits a different crystal structure when prepared through THF-casting. In particular, it shows that while peak 1 and 5 are enhanced, peaks 3 and 7 are considerably weakened (see Fig. S8a-b in supplementary information). Similar results were found for 15%HS, (see Fig. S8c-d). DSC confirms qualitatively this result by showing the fall of the broad melting peak originally present around T_m-30 °C, evidencing the polymorphic nature of the T4T crystallites. Additional evidence of polymorphism was also found in Flash DSC experiments and will be reported in another publication [30].

3.2.2. *Emerging scenario: formation of ribbons*

A way to interpret such WAXS patterns is to go back to the T4T structure presented in Fig. 1. It suggests that the crystallization can occur via the N-H and C=O groups in a similar fashion as in the Nylon-4,T [31] or in the popular aliphatic Nylon-6 and -66 in which the most stable phase is known as α and corresponds to the anti-parallel stack of the polymer chains [9]. Interestingly, both aromatic and aliphatic Nylons seem to provide similar WAXS patterns most likely due to their common H-bonds driven structure [31a].

Besides, the succession of the functional groups likely leading to H-bonding in T4T is the following: [C=O - N–H -(C_x)- N–H - C=O] by analogy with the Nylon- 66 [32] and in opposition with Nylon-6 in which the motif is [N–H - C=O -(C_x)- N–H - C=O] [33] (see also Fig. S7 in the supplementary information). This excludes therefore the presence of the γ phase corresponding to the parallel configuration stack of the chains as described in the Nylon-6 [34].

Table 2
Position of the diffraction peak as found in Fig. 3 and comparison with the literature about Nylon's α-phase and π-π stacking. The slight discrepancies are likely due to the fundamental differences between the Nylon-4,T, Nylon-66 and the T4T respective architectures as well as the presence of the SSs.

Peak	2θ (°)	Position in T4T crystallites (nm^{-1})[a]	Position in the literature (nm^{-1})	Characteristic distance (nm)[b]	Identification
1	6.48	4.6	4.75 [36] – 4.76 [35]	1.36	Inter T – α_{001}
2	10.8	7.7	7.1 [35]	0.81	α_{002}
3	17.9	12.7	12.8 [36,37]	0.49	Tr π - π
4	19.8	14	–	0.45	Amorphous halo
5	21.9	15.5	14.3 [35]	0.41	α_{100}
6	23.4	16.5	16.2 [31a]–17 [35]	0.38	α_{010}
7	25.3	17.8	17.2 [35]	0.35	α_{110}
			17.9 [36,37]		*P π- π?*
8	29.5	21.0	20.8–22.4 [31b]	0.30	N–O also seen in Ref. [25]

[a] The peak positions come from the tentative of deconvolution of the 20%HS diffractograms presented in supplementary information Fig. S8a–d.
[b] The characteristic distances correspond to 2π/"position in T4T crystallites". In the last column, the Miller indices refer to the crystallite axis in the following order: LWH (see Fig. 4).

Interestingly, Bunn and Garner [32] also reported that a so-called β-phase, similar to the α one in terms of WAXS pattern, could rise from the intermolecular H-bonds bending. Hence, starting from the diffraction pattern of the (aromatic and aliphatic) Nylon's α-phase, one can already identify several peaks obtained from our T4T crystallites (see Table 2). It is notably the case for the peaks 1, 2, 4, 5 and 6 for which positions are found to be in good agreement with the literature [31,35]. The peak 1, also visible in the high-q range of the SAXS experiment in Fig. 4a, refers to the inter-T groups distance belonging to a same Nylon 4-T chain [36], i.e. the distance between the two aromatic rings within the T4T unit (noted α_{001}). The peak 2 has the same origin. Since the peak 4 is not present in the HS precursor but it appears in the pure SS, we assign it to the inter-chain distance, i.e. to the usual amorphous halo present in polymers. We then believe that the peak 5 stands for the HS stacking in the H-bond direction (noted α_{100}) and grows significantly when THF casting is used (longer crystallites, see discussion in section 3.4). Finally the peak 6, greatly hidden by the previous one, must correspond to the HS stacking in the perpendicular direction (noted α_{010}) and peak 8 is assigned to the N–O distance within one H-bond.

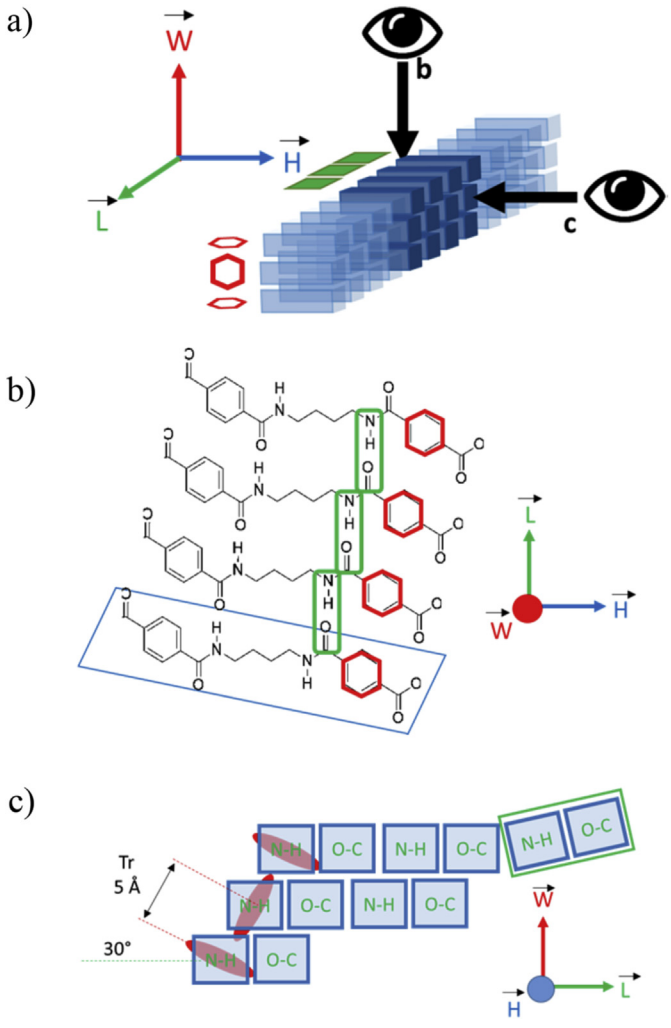

Fig. 4. Cartoon representing the structure of a crystallite piece. The green polygons represent the H-bonds while the red ones stand for the aromatic rings. a) 3D view, the black arrows indicate the view direction in b) and c), b) top view, c) side view. (For interpretation of the references to colour in this figure legend, the reader is referred to the web version of this article.)

Determining the origin of peaks 3 and 7 is more delicate. The fact that they are strongly weakened in the THF-casted sample and that this goes along with a large reduction of the first broad melting peak in DSC (see the inset of Fig. 3b) suggests that they correspond to a weaker structure, which is apparently not favored when the chains have a larger mobility, e.g. during the solvent casting procedure. Looking further at the T4T unit, it is interesting to investigate, apart from the amide groups, the possible role of the two aromatic rings. These groups make the HSs intrinsically very rigid and can easily lead to associations via π-π stacking, as it has been observed in a wide variety of systems in the literature (see below). They can therefore increase the HSs coordination number (e.g. allowing the crystal to grow in 2D) i.e. with the H-bonds aligned along one given direction and the π-π interactions perpendicular to it. In fact, the strong H-bonds (≈10 kJ/mol each) could even promote this π-π stacking by bringing the HSs close to each other obliging them to pack in a way that suits the excluded volume of aromatic rings (see Fig. 4). The resulting probability to form π-π stacking should consequently be larger in these particular TPEs than in other H-bonds free ones like polybutylene terephthalate [37]. To summarize, we believe that this second degree of freedom is most likely at the origin of the complex HS lattice because it induces a two-unidirectional crystallization from two distinct molecular interactions.

In order to validate this scenario, one needs to look at the possible configurations for neighboring aromatic rings and see if they are consistent with the peaks 3 and 7 observed in the WAXS pattern. Two possible configurations are reported in the literature known as “Tr” (transverse) and “P” (parallel) with respective distances between the rings' centers of mass being approximately 5 and 3.5 Å and bonding energy close to 0.72 and 0.48 kJ/mol [38]. Interestingly, these particular distances have been reported from WAXS experiments in both biological and synthetic polymers [39] containing aromatic groups while they do not appear in “rings-free” polyamide [35]. The latter observations seem therefore to confirm the nature of the peak 3. The nature of the peak 7 remains more uncertain since apart from the P rings configuration, it could also very well fit with the α_{110} diffraction for which a decrease of the ribbon thickness would also lead to a weaker intensity.

We provide in Fig. 4 a tentative cartoon summarizing our ideas on the T4T crystal lattice. Within this picture, we finally conclude that the length of the ribbons is governed by the “fast” and strong H-bonds while their thickness is influenced by the “slower” and weaker π-π stacking between the “1D-sheets” of associated HSs. Beyond the structure, this last results allows to rationalize the broad melting peak observed in DSC in terms of progressive “unstacking” of the HS sheets before their final melting (H-bonds rupture).

In order to investigate the shape of these ribbons at higher lengthscale (>2 nm), SAXS measurements are then needed, as discussed in section 3.3.

3.3. Multiscale structure – SAXS

3.3.1. Definition of the elementary HS building-block

The length of one elementary HS can easily be estimated by considering the distances between the atoms and the angles between the bonds as well as the aromatic rings size (see Fig. 1), and by accounting for the fact that the conformation induced by the two H-bonds and possible π-π stacking in each segment is stretched. This leads to a HS length of $H = 2.1$ nm.

On the other hand, determining the exact cross-section of the HS is not obvious. Indeed, the four carbon atoms between the two amide groups are in principle able to slightly bend or rotate inducing a degree of freedom in the crystallite leading to its ribbon-

like shape. Consequently, it is *a priori* difficult to know, whether two consecutive aromatic rings belong to the same plane or not. Therefore, for simplicity, we regard the HS as a square based parallelepipedic object having square cross section with $R = 0.5$ nm being the side (equivalent to the diameter of the aromatic ring accounting with the H atoms). As shown in Fig. 4, the angle between the H-bond plane (amide group) and the aromatic ring has been reported being around 30° in Nylon-4,T [31b], it does not however impact our analysis here.

From the previous assumptions, we extract the volume of the HS building-block.

$V_{HS} = HR^2 = 0.53$ nm^3, the corresponding scattering intensity for $q \to 0$, $I_{HS}(0) = I^0_{HS} = \Delta\rho^{2\prime}V_{HS} = 0.49$ cm^{-1} and the radius of gyration $R_{g-HS} = \sqrt{\frac{1}{3}\left[\left(\frac{H}{2}\right)^2 + 2\left(\frac{R}{2}\right)^2\right]} = 0.64$ nm.

By further combining these expressions within the Guinier approximation [40], we can determine the single HS scattering intensity on a wider q-range, $P_{HS}(q)$ being the form factor of a single HS such as:

$$I_{HS}(q) = I^0_{HS}\ P_{HS}(q) \approx I^0_{HS}\ \exp\left(\frac{R^2_{g-HS}q^2}{3}\right) \quad (1)$$

The result of the previous calculation is plotted in Fig. 5a (black solid line). As expected, at high q, i.e. for $q \to q^{\#}$, $I_{HS}(q)$ becomes comparable with the experimental reduced intensity. This good agreement supports the approximations made on the T4T structure and on the normalization procedure (see section 2 in supplementary information).

3.3.2. Mesoscale organization (crystallites)

Once the single HS dimensions are well defined, we can analyze the TPEs structure at a larger, mesoscopic length scale, i.e. investigating the crystallites morphology. Note that the latter can be formed through the aggregation of HS units in the plane orthogonal to the local chain axis with their thickness being defined by the previously determined HS length H. The two other dimensions (width and contour length) are called in the following W and L, respectively. As explained in section 3.2, we believe that the H-bonds are parallel to the long axis of the crystallite ($\vec{L}$) [31b] while the weaker π-π stacking (Tr or P) is responsible for their width (W).

The total number of HS per crystallites N_{agg} is defined from the aggregation numbers (N_H, N_w, N_L) along each axis ($\vec{H}, \vec{W}, \vec{L}$), respectively, such as $N_{agg} = N_H N_w N_L = N_w N_L$ since N_H is fixed to 1 from the chemical structure (see Figs. 1 and 4).

The normalized scattering intensity measured by SAXS as a function of the transfer momentum q are presented in Fig. 5a for all the hot-pressed TPEs. The general trend of the spectra can be analyzed, looking at the different q-ranges (see also sections. 2.1 and 2.2 in supplementary information for further details on the data treatment, notably Φ_{eff}):

For $q > q^{\#}$, the X-rays see the matter as a discrete phase, we refer the reader to the WAXS experiments (see section 3.2) – a small peak around 4 nm^{-1} (1.57 nm) is nevertheless visible for the 20%HS and corresponds to the distance between the T units in the same chain [36]. Here, one can note that $q^{\#} \approx 3$ nm^{-1}, corresponding to $d^{\#} = 2\pi/q^{\#} = 2.1$ nm, which is in good agreement with the smallest dimension of a single HS defined above.

For $q_{cs} < q < q^{\#}$, the intensity is described by a power law ~ q^{-S} giving information on the local structure of the crystallites. This regime is known as the Porod regime. A value of S equal to 2 stands for a flexible object such as a polymer coil in θ-solvent [41], while a value of S equal to 4 is understood as a sharp interface (equivalent to a surface fractal dimension of 2, i.e. smooth objects like hard colloids [42]). The S values found for the four samples are given in Table 3. One can clearly see that these slopes evolve monotonically with the HS content passing from ≈2.0 (for 5%HS) to 3.7 (for 20% HS), i.e. from a flexible object to an object with a sharp interface.

At $q = q^*$, we observe a maximum, which can be attributed to the most probable distance between the center of mass of the

Table 3
Morphology of the crystallites at the mesoscale extracted from SAXS data for 5, 10, 15 and 20%HS. Their thickness is kept constant $H = 2.1$ nm.

%HS	Φ (%)[a]	q* (nm^{-1})	d* (nm)	S	W (nm)[b]	$N_w = W/R$
5	3.5	0.43	14.6	2.1	1.18	2
10	7.2	0.62	10.1	2.6	2.28	4
15	10.9	0.72	8.72	3.1	3.94	8
20	14.8	0.77	8.16	3.7	4.69	>9

[a] The values of Φ (volume fraction in HS) are calculated from equation (S2) (supplementary information).
[b] The calculation of W is made from model A for 5%HS and from model B for 15% HS and 20%HS. The corresponding value for 10%HS is calculated by averaging the results from model A and B (intermediate case).

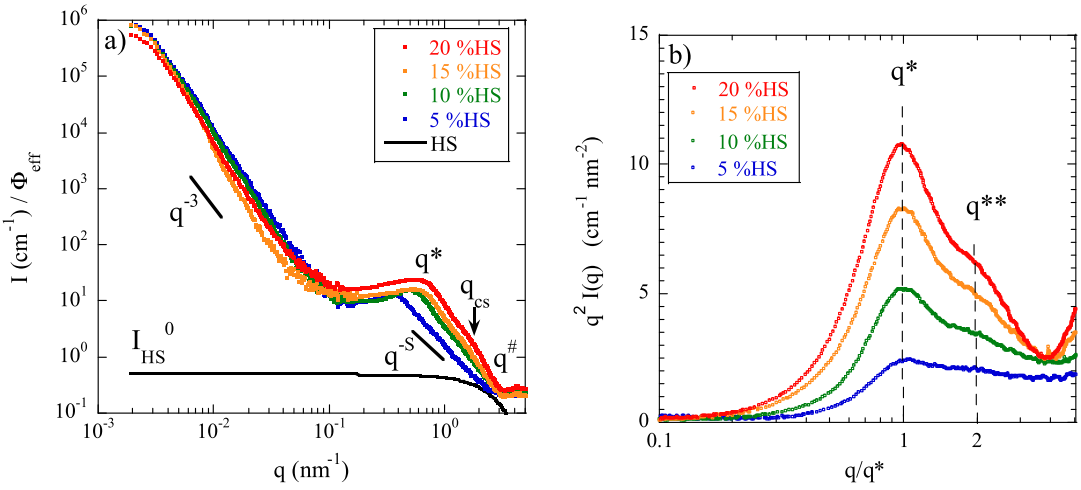

Fig. 5. a) Normalized scattering intensity measured in SAXS as a function of the transfer momentum q for the four segmented block copolymers containing 5, 10, 15 and 20%HS. The solid black line stands for the reconstruction of $P_{HS}(q)$ calculated in equation 1. b) Kratky representation ($I(q)q^2 = f(q/q^*)$) of the same data set. The characteristic distance between the crystallites is seen through q^* while the presence of $q^{**} = 2q^*$ suggests a lamellar phase. Note that q_{cs} in a) and q^{**} in b) have a similar value but different meanings (see text).

crystallites $d^* = 2\pi/q^*$, i.e. with the inter-crystallites structure factor $S_c(q)$. This distance between crystallites, d^*, is reported in Table 3. As expected, it decreases with increasing the HS volume fraction (or number density), which reflects the network densification.

(For q < q* we refer the reader to the sub-section entitled **Considerations on the structural features above *d**** presented later in the article.)

We can then plot this SAXS data using the Kratky representation [40] (see Fig. 5b.). Interestingly, normalizing the scattering vector by q^* reveals a second structural feature in the 10, 15 and 20%HS TPEs positioned at $q/q^* = 2$. This is typical of a lamellar organization [43], and suggests the presence of crystallites stacks, i.e. anisotropic structure from the d^* length scale, which becomes more pronounced when increasing the volume fraction of HS.

By combining this result to the Porod exponent S, we propose the following picture: The Porod exponent having a value close to 2.0 in the 5%HS sample suggests that the crystallites can be seen as thick polymers in θ-solvent, i.e. as objects having non-zero thickness H and width W following a random walk that, by definition, leads to an isotropic morphology. On the contrary, within the same q-range, the Porod exponent for the 20%HS is 3.7 and the intensity shows a shoulder at $q = q^{**} = 2q^*$ suggesting the formation of a lamellar structure in which the crystallites have thus the same orientation (at the mesoscale), leading to an anisotropic morphology. These two extreme cases are represented in Fig. 6 by the morphology A and the morphology B. Between these two samples, the intensity scattered by the 15%HS TPE is close to the 20%HS one (see. Fig. 5a) suggesting therefore that the morphology B should stand. The situation is more ambiguous for the 10%HS because it shows a distinct scattering pattern from both 5%HS and 15%HS with $S = 2.6$ implying an intermediate structure.

3.3.3. Determination of the width of the crystallites (W) and 3D arrangement

Because of these drastic changes in the TPEs structure with the reduction of the pTHF soft-segments in the copolymer chains, we propose to use these two simple albeit plausible geometrical models in order to describe the average situation in a volume element of the TPEs and to determine the corresponding width of the crystallites, W_A and W_B:

A) The crystallites form a network based on a soft cubic cell for which each edge is made of a free crystallite segments with their length being in average d^*. The decrease of d^* with increasing Φ is understood as the shrinkage of this 3D "isotropic" soft cage (no preferential direction as seen in Fig. 6a) when the number of crystallites increases in the sample.

B) The crystallites are all aligned along the same axis $\vec{L}$ and separated by a distance d^* corresponding to the cell parameter of a square lattice similarly to the hexagonal packing used by Sijbrandi et al. [13]. In this case, the decrease of d^* with increasing Φ is understood as the shrinkage of a 2D "locally" ($\approx$10 nm) anisotropic square lattice belonging to the plane $(\vec{H}, \vec{W})$ and therefore orthogonal to the crystallite long axis. In this suggested model, the volume fraction Φ is equivalent to a surface fraction Φ_s in the plane $(\vec{H}, \vec{W})$.

Considering that the HS volume fraction (or surface fraction in model B) in one cell is equivalent to the HS volume fraction Φ in the whole sample, one can easily express the HS volume fraction in one cell for A and B morphologies as: $\Phi = N_n HW/d^{*2}$ with N_n being the number of full objects to be considered per lattice giving $N_A = 12 \times 1/4 = 3$ and $N_B = 4 \times 1/4 = 1$. Besides, assuming $H = 2.1$ nm as estimated in the precedent section, one can then simply extract the width of the crystallites (reported in Table 3) from each model, only differing by construction by a factor 3 such as: $W_A = W_B/3 = \Phi d^{*2}/3H$.

While for the 15%HS and 20%HS samples, the morphology B is used, we consider the morphology A for the 5%HS sample, and an average of the two for the 10%HS sample, which lies between these two extremes. It must be noted that the values of W are found to be in good agreement with the one reported by van Hutten et al. from the analysis of the breadth's peaks from WAXS experiments [25].

From these values and from the estimated size of an elementary HS building block, one can determine the corresponding number of HS in the width direction $\vec{W}$, N_w, as reported in Table 3. While the lateral packing of the HS is rather limited at low volume fraction of HS, it becomes quite important at larger density. This can be understood by considering the reduced mobility and enhanced proximity of the crystallites at high volume fraction of HS, which are forced to organize into a lamellar structure.

3.3.4. Evolution of ribbon-ribbon distance (d*) with the HS volume fraction

The morphology of the crystallites is strongly influenced by the HS volume fraction. It is therefore interesting to investigate how d^* evolves with Φ, and see if its evolution is well described by the picture proposed above, according to which the morphology of the ribbons evolves from the geometrical model A at low HS volume fraction, to the model B at larger fraction. The evolution of d^* with

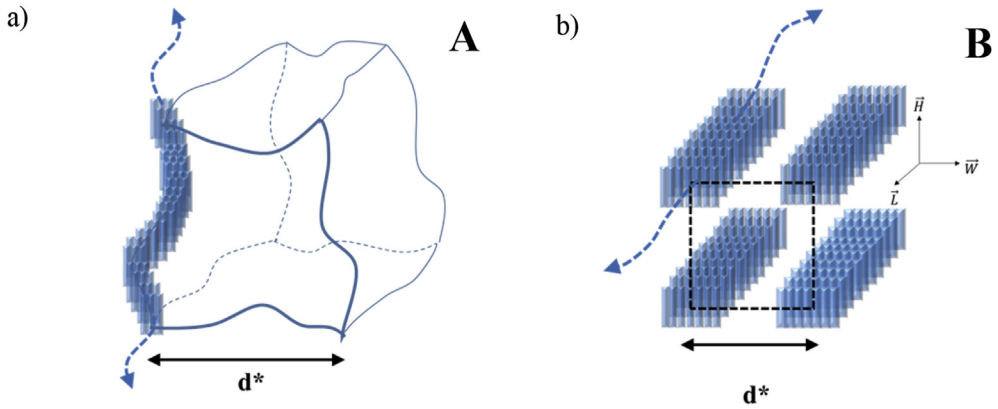

Fig. 6. a) 3D isotropic model (denoted as A) and b) 2D locally anisotropic model (denoted as B) describing two possible arrangements of the crystallites leading to different evolutions of the inter-crystallites distance when %HS is changed. In both cases, dashed arrows stand for the (curvi)linear long axis of the crystallites.

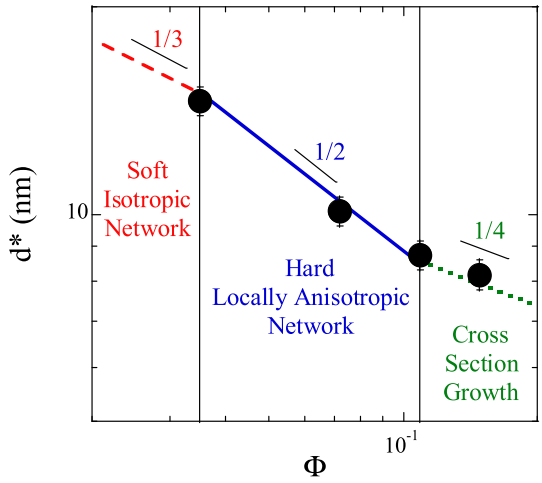

Fig. 7. Log-log representation of the most probable distance between the crystallites d^* as a function of the volume fraction in HS (Φ). The blue solid line is a power law fitted to the data with the exponent being fixed to 1/2. Red and green dashed lines are power law with respective exponent 1/3 and 1/4 and serve as guide for the eyes, they are related with the interpretation in the text. (For interpretation of the references to colour in this figure legend, the reader is referred to the web version of this article.)

the HS volume fraction Φ is shown in Fig. 7. From basic geometrical arguments, we know that this function can be written as the following: $d^* = P\Phi^{-1/h}$ where P is related to the object size (see below), and h is the spatial dimension of the "problem" satisfying $[h] = m^h$. For instance, it is well known that for a homogeneous colloidal suspension the distance between the particles centers of mass evolves with $\Phi^{-1/3}$, i.e. $h = 3$ [44].

In our case, as shown in Fig. 7, it appears that $h \sim 2$ between 5 and 15%HS. This suggests that the distance between the objects evolves in a similar way as in a 2D space, which is in good agreement with the proposed geometrical model B, and which confirms the anisotropic nature of the crystallites network at high HS content. Below 5%HS, we believe that the softness of the crystallites ($S = 2$) and the absence of peak at $q/q^* = 2$ in Fig. 5b should lead to a soft isotropic network (i.e. $h = 3$). In Fig. 7, we also observe that the value of h between 15 and 20%HS is greater than 3 (close to 4) indicating that most of the additional HS units (from 15 to 20%HS) do not lead to the formation of new crystallites (which would make the inter-crystallites average distance d^* weaker) but rather contribute to the growth of the already existing ones. This result is further supported by the very similar patterns measured for the 15 and 20%HS in Fig. 5a where the slightly higher value of S (Table 3) stands for an even sharper object with a probable enhanced lamellar order.

In addition to the value of h, the above mentioned expression of d^*, provides us with the prefactor of the 1/2 power law in Fig. 7, estimated to be $P = 2.8$ nm. In a 2D problem, and considering a square lattice as in the model B, one can relate its value to the geometry of the crystallites $P = \sqrt{HW_B}$ allowing then to highlight the good agreement with the value of W for 15%HS (see Table 2): $W_B = P^2/H = 3.73$ nm. Note that in order to compare the values of W from the two calculations (from P and d^*), the model B needs to be valid (anisotropy) and the thickening of the crystallites due to a high HS loading must not be significant (i.e., among our samples, this comparison can only be done for 15%HS).

3.3.5. Cross section radius of the crystallites

Furthermore, one can also refer to the change in slope observed for the 20%HS sample in Fig. 5a at $q = q_{cs}$. This singularity (with matches in this case with $2q^*$), particularly visible for rigid objects, denotes the transition from the Porod regime to the fractal regime, giving information on the cross section radius of the crystallites $R_{cs} = \pi/q_{cs}$.

In order to validate the morphology picture given by the geometric model B, it is then possible to compare the experimental q_{cs} value of the 20%HS sample with the one derived from the model by approximating the equivalent cross section radius $R_{cs}^{(B)}$ from H and W_B (true rectangular cross-section) such as: $S_{CS} = HW_B \approx \pi R_{cs}^{(B)2}$ where S_{CS} is the average cross section of the crystallites in the 20%HS TPE. We then directly get the corresponding value for $q_{cs}^{(B)}$ that is reported with a black arrow in Fig. 5a: $q_{cs}^{(B)} = \frac{\pi}{R_{cs}^{(B)}} = \frac{\pi\sqrt{\pi}}{\sqrt{HW_B}} = 1.77\ \mathrm{nm}^{-1}$. Again, a good agreement in found, further reinforcing our data interpretation at the mesoscale.

All the previous analysis suggests thus strongly that, above 10% HS, the crystallites are locally oriented along a given $\vec{L}$ axis forming a structure close to a 2D anisotropic lamellar phase (model B). This meso-scale anisotropy, which undoubtedly has to do with the rigidity of the crystallites, has been pointed in numerous papers in which AFM clearly revealed the orientation of the objects for distances between ≈10 and 100 nm [6a,17,45]. It must be noted however that at a higher length scales (i.e. for $d \gg d^*$), this anisotropy is lost due to the flexibility of the ribbons, reminding the behavior of soft polycrystalline materials [46]. In the next section, we give arguments to speculate about a methodology to extract structural features at distances greater than d^* e.g. the "volume" fractal dimension of the crystallite D_f and its growth mechanism.

3.3.6. Considerations on the structural features above d^*

For $q < q^*$, as shown in Fig. 4, the scattering intensity seems to saturate (plateau). At first sight, one could interpret this by the presence of objects with a well-defined mass. However, this plateau should be rather seen as the product of the crystallite average form factor $P_c(q)$ and the "correlation hole" usually seen in structure factors for $q < q^*$ [47] such as:

$$I(q<q^*) = I_0 P_c(q<q^*) S_c(q<q^*) \quad (2)$$

with $I_0 = \Phi\Delta\rho^{2\prime}$ and $\langle P_c(q<q^*)\rangle = V_c q^{-D_f}$ where V_c is the average volume of a crystallite and D_f the fractal dimension of the crystallites which must satisfy $1 < D_f < 2$ for semi-rigid rod-like objects.

Finally for $q < q^*$, the scattering intensity follows a power law $I(q) \sim q^{-3}$ which can hardly be interpreted in terms of structure (e.g., infinitely dense agglomerates of crystallites). While the origin of such a low-q upturn is not well understood, we believe that it could come from multiple-scattering, possibly limited by using thinner samples.

As previously mentioned, the scattering intensity results in structural features related to the shape and size of the scattering objects (form factor) as well as their respective position from each other (structure factor). While the presence of characteristic distances were expected at molecular (crystal lattice visible in WAXS) and mesoscopic (inter-ribbons distance visible in SAXS) length scales, the lack of organization at larger distances (like in smectic phases [48]) inhibits the direct extraction of structural features through the observation of the emerging structure factor (i.e. scattering peaks). Even "worse", the contribution of the unknown large-scale structure factor within the total scattering intensity $I(q)$, makes impossible the identification of the crystallite morphology via their average form factor $P_c(q)$. In the literature, the latter is often measured independently. For example, in nanocomposites or suspensions based on well-defined objects such as hard-spheres, it is directly obtained by measuring samples in which Φ is kept low (typically below 1 vol%, where the structure factor is negligible

[49]). For more complex industrial nanofillers, a way to proceed, as recently suggested by Baeza et al. [50], is to dilute a posteriori solid samples through an in-situ polymerization process passing from $\Phi = 20$ vol% to roughly 2 vol% with keeping the same filler morphology. However, since the shape and the size of the crystallites present in our TPEs are intimately related with the HS content, none of these methods can be applied here.

A reliable way to study the large-scale structure resides in studying the TPEs starting from high temperature ($T > T_m$) to low temperature, i.e. starting at temperature at which the crystallite fraction is low enough so that it is possible to extract information about their average form factor. To do so, we performed time-resolved SAXS experiments with temperature control on the 20% HS sample on the beamline DUBBLE at ESRF. The result, similar to the one by Versteegen et al. [51] is presented in Fig. 8 and allows to highlight several important points:

(i) $\boldsymbol{T \geq T_m \approx 170}$ **°C.** Despite the fact that the sample is in the melt state, a significant X-ray scattering is measured. This indicates that the HSs are not fully dispersed, i.e. that a fraction of H-bonds, still active, leads to clusters formation. One can here use the Guinier approximation (equation (1)) to fit the shoulder observed at 0.7 nm^{-1} allowing to quantify these objects with a typical radius $Rg^{Tm} = 1.8$ nm and an aggregation number $N_{agg}(T_m) = I_G^{T_m}/I_{HS}^0 \approx 18$. Interestingly, the fact that $\pi/Rg^{Tm} \approx q_{cs}$ means that, those persistent aggregates have a radius of gyration similar to the cross-section one of the crystallites formed at low temperature. This feature thus strongly suggests that the latter are made of a train-like stacks of the former. Besides, their presence explains the "non-Maxwellian" rheological behavior observed at $T = T_m$+10 °C in (see Fig. S10 in supplementary information) where $G'(\omega)$ in particular, exhibits a power law behavior with an exponent significantly lower than 2, indicating the presence of association points ("stickers") between the chains.

(ii) $\boldsymbol{T_m > T > 167}$ **°C (t = 25 s of cooling – see Fig. 8b).** As soon as the temperature starts to decrease, the scattering intensity evolves at low angle ($q < 1$ nm^{-1}) due to the formation of larger objects through the supramolecular bonds which become statistically more likely to exist. In this regime, we believe that the interactions between the growing scattering objects are still negligible. Indeed, no structural peak, i.e. shoulder or maximum, is observed, suggesting that the total scattering intensity must be proportional to the average form factor of the crystallites $I(q) \sim P_c(q)$. Nevertheless, as expected, decreasing the temperature leads to bigger and bigger structures characterized by a growing fractal dimension D_f from ≈0 (finite persistent aggregates) at T_m to ≈1.2 at 167 °C (after 25 s of cooling). Interestingly, the latter value, reflects the rod-like shape of the crystallites before they start to stack, in good agreement with the previously proposed model B (see. the black dashed line Fig. 8b).

(iii) $\boldsymbol{T < 167}$ **°C.** A clear maximum standing for the inter-crystallites distance starts to appear at q^* (see Fig. 8b). The fall of the scattering intensity at $q < q^*$ when the temperature is decreasing, i.e. when the crystallites are growing ($P_c(q)$ increases), is thus unambiguously related with the appearance of the structure factor "correlation hole". From this point, $I(q) \sim P_c(q)S_c(q)$. Further decreasing of the temperature (i.e. t > 25 s) leads to the deepening of the correlation hole together with the shift of the "q^*-peak" towards higher q. The latter confirms therefore the densification of the crystallites network until T reaches ≈136 °C (t = 255 s) at which $I(q)$ saturates, in good agreement with the crystallization temperature T_c determined from DSC. Finally at $T < T_c$, the dynamics are "frozen" for $d > d^*$.

3.4. Tentative mechanism of HS crystallite growth

Based on the structural results from the previous section and on the tests realized on solvent casted samples, we propose here a tentative growth mechanism for the HS crystallites, as illustrated in Fig. 9 below.

First, we recall that the crystallization of the HS in TPEs is predominantly driven by the strong attraction due to the H-bonds created through the amide groups of these short units (2.1 nm – see section 3.3.1), which in turn dictates their spatial organization. This is akin to microphase separation in block copolymers, where the domains of the hard block form a crystalline order such as in rod-coil copolymers [52]. In the absence of H-bonds, given the small size and relatively low amount of HS within a chain, a homogeneous amorphous melt should result at $T > ODT$ (order disorder temperature). This H-bond driven process (and the well calibrated HS size) likely explains the high crystallization rate and the corresponding high crystal fraction (≈70% of the HS, see Table 1).

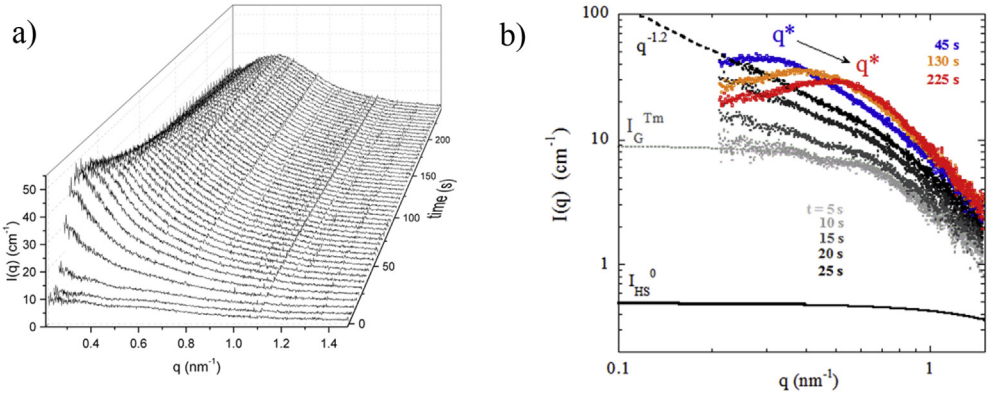

Fig. 8. a) Reduced scattering intensity as a function of the momentum transfer q for the 20%HS sample with varying the temperature from 170 °C to 40 °C at ≈8 °C/min b) Selection of intensity profiles at given cooling times. The grey data are measured during the first 30 s of the test ($I(q) \sim P_c(q)$) while the colorful ones are obtained from 1 to 5 min ($I(q) \sim P_c(q)S_c(q)$). This data set has been rescaled to the corresponding intensity shown in Fig. 5a in order to access the absolute units (procedure described in supplementary information section 2.3). The dashed line is fitted to the data with the Guinier approximation in order to extract the radius of gyration and the aggregation number of the scattering objects present at $T = 170$ °C. The black solid line stands for $I_{HS}(q)$. (For interpretation of the references to colour in this figure legend, the reader is referred to the web version of this article.)

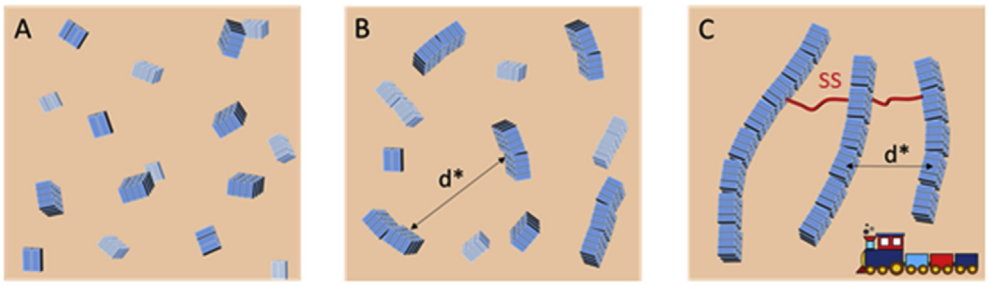

Fig. 9. Growth mechanism of the HS crystallites with decreasing temperature. The blue objects stand for the HS and the red background for the SS. a) Melt state at T > T_m. b) Agglomeration of the persistent aggregates at T ≤ T_m. c) "Train" growth and orientation of the crystallites resulting in a "frozen" structure at the mesoscale when T_c is reached. (For interpretation of the references to colour in this figure legend, the reader is referred to the web version of this article.)

Starting from the melt state (T > T_m ≈ 170 °C), it appears that the probability to form H-bonds (crystal) or, to phase separate (amorphous), is non-zero (Fig. 8b), leading to the formation of the above mentioned persistent aggregates (Fig. 9a). At this temperature, these small clusters are in equilibrium with isolated building blocks, in an analogous fashion to systems like living polymers [53]. Those aggregates, typically made of 18 HSs (with $Rg^{Tm} = 1.8$ nm) are nevertheless too few to interact with each other (no structure peak in Fig. 8b). By following the viscoelastic properties of these TPEs through time at this high temperature, we also observed that the number density of these aggregates slowly increases with time, but are not forming crystallites yet [30]. Decreasing the temperature below T_m enhances the strength of attraction (e.g. H-bonds shortening [54]), hence, the probability to form bigger clusters via H-bonding and other interactions such as π-π stacking (Figs. 5 and 9b). While the former leads to a growth of the clusters (crystallites) along $\vec{L}$, the latter will cause their thickening along $\vec{W}$ (see Fig. 6). The net result is the formation of elongated ribbons as evidenced in Fig. 8b through the evolution of their fractal dimension (dI(q)/dq) from 0 to 1.2 (Table 3). Interestingly, Fig. 8b also reveals that the position of the form factor shoulder (at $q \approx 0.7$ nm^{-1}) remains constant with the time suggesting that the cross section of these growing objects does not evolve significantly during the cooling phase. This implies that the early stage of crystallization is characterized by the presence of small isotropic objects which will associate along $\vec{L}$ such as train's wagons with decreasing the temperature (Fig. 9c).

Upon further decrease of temperature, the growing anisotropic objects start to interact with each other, giving rise to a broad structure factor peak positioned at q^*, typical of soft potentials. In this situation, $d^* = 2\pi/q^*$ is the most probable inter-object distance. While at low-HS content this soft interaction is akin to that of wormlike chains, at high-HS content we expect orientational order. Indeed, as indicated in Tables 1 and 3, the average number of HS per chain is three times higher for 20%HS TPEs compared to 5%HS and the inter-object distance is about half, suggesting an enhanced tendency for alignment since in this way long ribbons will minimize their free energy (see Figs. 9c and 6b) in a similar fashion as what is found in anisotropic assemblies of peptides [55].

Finally, the structure virtually freezes when the temperature approaches T_c. In this case, the crystallites are essentially trapped in a region of space around d^* consisting of two potential walls generated by the SSs which can fluctuate between W and $W + M$, where M is the length corresponding to a fully stretched SS.

In the above tentative picture, it is expected that the growth of crystallites and their final state depend on the initial conditions, i.e., on the initial relative positions of the HSs (since the interactions are directional) and on the possible presence of persistent aggregates.

On the other hand, as already mentioned, the crystal formation in the solvent-casted TPEs seems rather different than in the bulk, showing a strong decrease of the π-π interactions signature in DSC (secondary peak in Fig. 2) and WAXS (peaks 3 and 7 in Fig. 3). While in the hot-pressed samples, the previously proposed mechanism could be described as a "train growth" process due to the cluster stacking along $\vec{L}$ resulting in a constant cross section radius during the crystallization, one could imagine a fundamentally different but plausible scenario for solvent-casted samples, named "1D-sheet growth", to explain the multi-scale formation in these (room temperature) solvent-casted TPEs. This process would consists in the following. A low volume fraction of TPEs chains is well dispersed in a (polar) H-bond competitor solvent such as THF which is expected to provide a (quasi)single HS dispersion at the beginning of the experiment. During the evaporation of the solvent, because of the lower viscosity with respect to the hot-pressed case, the short range diffusion of the HS is enhanced allowing their systematic aggregation in the most preferential energetic way, i.e. via H-bonding (rather than π-π stacking). The crystallites can thus quickly grow along $\vec{L}$ until reaching a maximal viscosity (due to solvent evaporation and ribbon growth working together) at which long 1D-sheets are fully formed and "freeze" the system. They will then hardly stack on each other because of big entropic penalty resulting notably in a strong decrease of the π-π interactions signature in DSC or WAXS together with a higher order in the long axis direction (see peak 5 in Fig. 3b and Fig. S8b).

4. Conclusions

In this article we have undertaken a thermal and structural study of segmented TPEs synthesized by polycondensation of T4T (hard segment) and pTHF (soft segment) units by means of DSC, WAXS and (U)SAXS. The effect of the hard-segments content has been investigated on four different hot-pressed samples containing 5, 10, 15 and 20%HS. DSC revealed a strong increase of the terminal melting point from 90 to 160 °C jointly with the apparition of a secondary melting peak situated at ≈ T_m−30 °C when the HS content was increased from 5 to 20%. The latter was however eliminated when the sample was prepared through THF-casting, emphasizing the importance of the sample preparation. Molecular scale (1 Å - 1 nm) WAXS experiments have confirmed the polymorphism in hot-pressed TPEs and unambiguously revealed the presence of π-π stacking interactions in addition to the well-known H-bonds in polyamide-based systems. At larger length-scales (1–30 nm), SAXS experiments have simultaneously shown a decrease of the inter-crystallites distance with a raise of their local rigidity, leading partly to a lamellar order, when the hard-segment mass fraction was increased above 10%. These results have been interpreted through two geometrical models, representing the average local situation throughout the whole sample. This allowed

to estimate the width of the ribbon-like objects passing from 2 to 9 elementary T4T units, conforming to the above mentioned enhanced rigidity. Besides, time resolved SAXS measurements as a function of the temperature have highlighted the presence of persistent HS aggregates at $T > T_m$, which is believed to be at the origin of the slow relaxation that we observed in the terminal regime of the rheological response. Moreover, at larger length-scales (>30 nm), it allowed us to extract the "volume" fractal dimension of the T4T-crystallites (being close to 1.2), evidencing the quite rigid nature of the elongated objects present in the TPEs when the HS content is 20%. Based on this structural evolution we finally gave arguments on the growth mechanism highlighting once again the importance of the initial conditions, i.e. the shaping process.

All in all, the final properties of these thermoplastic elastomers depend strongly on their microstructure, which is largely influenced by different inter-related processes such as phase separation, hydrogen bonding, crystallization or π-π stacking, as well as by the density of HS, which influences the mescoscale organization of the crystallites. This provides an unprecedented tunability at molecular level, hence a better control on their final properties such as their toughness or melting properties. The latter will be investigated in a future work.

Author contributions

The manuscript was written through contributions of all authors. All authors have given approval for the final version of the manuscript.

Notes

The authors declare no competing financial interest.

Acknowledgements

We are grateful to Anne-Caroline Genix (L2C) and Michael Sztucki (ID02 beamline at ESRF) as well as Wim Bras (from the DUBBLE beamline at ESRF) for the SAXS data respectively measured on the beamlines ID02 and DUBBLE at the ESRF, Grenoble, France. GPB and AL are also indebted to Lampros Papoutsakis (FORTH) for his help with WAXS experiments. Enlightening discussions with Nicolas Alvarez (Drexel University) are gratefully acknowledged. Financial support has been provided by the EU FP7 (ETN Supolen GA-607937).

Appendix A. Supplementary data

Supplementary data related to this article can be found at http://dx.doi.org/10.1016/j.polymer.2016.11.010.

References

[1] N.R. Legge, Thermoplastic elastomers, Rubber Chem. Technol. 60 (3) (1987) 83–117.
[2] B. Adhikari, D. De, S. Maiti, Reclamation and recycling of waste rubber, Prog. Polym. Sci. 25 (7) (2000) 909–948.
[3] M. Cloitre, D. Vlassopoulos, Block copolymers in external fields: rheology, Flow-induced phenomena, and applications, in: Applied Polymer Rheology: Polymeric Fluids with Industrial Applications, J. Wiley & Sons, 2011, pp. 209–239.
[4] G. Holden, H.R. Kricheldorf, R.P. Quirk, Thermoplastic Elastomers, Hanser, Munich, 1996.
[5] L. Leibler, Theory of microphase separation in block Co-Polymers, Macromolecules 13 (6) (1980) 1602–1617.
[6] (a) W.P.J. Appel, G. Portale, E. Wisse, P.Y.W. Dankers, E.W. Meijer, Aggregation of ureido-pyrimidinone supramolecular thermoplastic elastomers into nanofibers: a kinetic analysis, Macromolecules 44 (17) (2011) 6776–6784;
(b) R.M. Versteegen, R. Kleppinger, R.P. Sijbesma, E.W. Meijer, Properties and morphology of segmented copoly(ether urea)s with uniform hard segments, Macromolecules 39 (2) (2006) 772–783.
[7] (a) J.A. Miller, S.B. Lin, K.K.S. Hwang, K.S. Wu, P.E. Gibson, S.L. Cooper, Properties of polyether polyurethane block copolymers - effects of hard segment length distribution, Macromolecules 18 (1) (1985) 32–44;
(b) C. Eisenbach, M. Baumgartner, C. Günter, Polyurethane elastomers with monodisperse segments and their model precursors: synthesis and properties, in: J. Lal, J. Mark (Eds.), Advances in Elastomers and Rubber Elasticity, Springer US, 1986, pp. 51–87.
[8] R.J. Gaymans, Segmented copolymers with monodisperse crystallizable hard segments: novel semi-crystalline materials, Prog. Polym. Sci. 36 (6) (2011) 713–748.
[9] S. Dasgupta, W.B. Hammond, W.A. Goddard, Crystal structures and properties of nylon polymers from theory, J. Am. Chem. Soc. 118 (49) (1996) 12291–12301.
[10] A.C.M. vanBennekom, R.J. Gaymans, Amide-modified poly(butylene terephthalate): Polycondensation, Polymer 37 (24) (1996) 5439–5446.
[11] M. Van Der Schuur, E. van der Heide, J. Feijen, R.J. Gaymans, Structure–property relations of segmented block copolymers with liquid–liquid demixed morphologies, Polymer 46 (11) (2005) 3616–3627.
[12] A. Arun, K. Dullaert, R.J. Gaymans, The melt rheological behavior of AB, ABA, BAB, and (AB)(n) block copolymers with monodisperse aramide segments, Polym. Eng. Sci. 50 (4) (2010) 756–761.
[13] N.J. Sijbrandi, A.J. Kimenai, E.P.C. Mes, R. Broos, G. Bar, M. Rosenthal, Y. Odarchenko, D.A. Ivanov, P.J. Dijkstra, J. Feijen, Synthesis, morphology, and properties of segmented poly(ether amide)s with uniform oxalamide-based hard segments, Macromolecules 45 (9) (2012) 3948–3961.
[14] D. Husken, J. Feijen, R.J. Gaymans, Hydrophilic segmented block copolymers based on poly(ethylene oxide) and monodisperse amide segments, J. Polym. Sci. Pol. Chem. 45 (19) (2007) 4522–4535.
[15] B.B. Sauer, R.S. McLean, R.J. Gaymans, M.C.J.E. Niesten, Crystalline morphologies in segmented copolymers with hard segments of uniform length, J. Polym. Sci. Pol. Phys. 42 (9) (2004) 1783–1792.
[16] M. Van der Schuur, R.J. Gaymans, Segmented block copolymers based on poly(propylene oxide) and monodisperse polyamide-6,T segments, J. Polym. Sci. Pol. Chem. 44 (16) (2006) 4769–4781.
[17] G.J.E. Biemond, J. Feijen, R.J. Gaymans, Poly(ether amide) segmented block copolymers with adipic acid based tetraamide segments, J. App. Polym. Sci. 105 (2) (2007) 951–963.
[18] I.W. Hamley, V. Castelletto, Small-angle scattering of block copolymers in the melt, solution and crystal states, Prog. Polym. Sci. 29 (9) (2004) 909–948.
[19] H. Benoit, G. Hadziioannou, Scattering-theory and properties of block copolymers with various architectures in the homogeneous bulk state, Macromolecules 21 (5) (1988) 1449–1464.
[20] J.S. Pedersen, P. Schurtenberger, Scattering functions of semiflexible polymers with and without excluded volume effects, Macromolecules 29 (23) (1996) 7602–7612.
[21] I.W. Hamley, J.S. Pedersen, C. Booth, V.M. Nace, A small-angle neutron scattering study of spherical and wormlike micelles formed by poly(oxyethylene)-based diblock copolymers, Langmuir 17 (20) (2001) 6386–6388.
[22] R.J. Gaymans, J.L. Dehaan, Segmented copolymers with poly(ester amide) units of uniform length - synthesis, Polymer 34 (20) (1993) 4360–4364.
[23] J. Krijgsman, D. Husken, R. Gaymans, Synthesis and properties of thermoplastic elastomers based on PTMO and tetra-amide, Polymer 44 (25) (2003) 7573–7588.
[24] R.J. Gaymans, S. Harkema, Melting behavior of aliphatic and aromatic diamides, J. Polym. Sci. Pol. Phys. 15 (3) (1977) 587–590.
[25] P.F. Vanhutten, R.M. Mangnus, R.J. Gaymans, Segmented copolymers with polyesteramide units of uniform length - structure-analysis, Polymer 34 (20) (1993) 4193–4202.
[26] B. Struth, K. Hyun, E. Kats, T. Meins, M. Walther, M. Wilhelm, G. Grübel, Observation of new states of liquid crystal 8CB under nonlinear shear conditions as observed via a novel and unique rheology/small-angle x-ray scattering combination, Langmuir 27 (6) (2011) 2880–2887.
[27] D. Pennicard, S. Smoljanin, B. Struth, H. Hirsemann, A. Fauler, M. Fiederle, O. Tolbanov, A. Zarubin, A. Tyazhev, G. Shelkov, H. Graafsma, The LAMBDA photon-counting pixel detector and high-Z sensor development, J. Instrum. 9 (12) (2014) C12026.
[28] L. Guang, R.J. Gaymans, Polyesteramides with mixtures of poly(tetramethylene oxide) and 1,5-pentanediol, Polymer 38 (19) (1997) 4891–4896.
[29] W.A. Lee, G.J. Knight, Ratio of the glass transition temperature to the melting point in polymers, Brit. Polym. J. 2 (1) (1970) 73–80.
[30] Sharma, A., Manuscript in preparation.
[31] (a) R.J. Gaymans, The synthesis and some properties of nylon 4,T, J. Polym. Sci. Polym. Chem. Ed. 23 (5) (1985) 1599–1605;
(b) J. Brisson, J. Gagné, F. Brisse, Model compounds of aromatic nylons. 3. The conformation of the 4T Nylon, poly(tetramethylene terephthalamide), using X-ray diffraction, solid-state 13C nmr spectroscopy and ir spectroscopy, Can. J. Chem. 67 (5) (1989) 840–849.
[32] C.W. Bunn, E.V. Garner, The crystal structures of two polyamides ('Nylons'), Proc. R. Soc. Lond. A Math. Phys. Eng. Sci. 189 (1016) (1947) 39–68.
[33] R.F. Stepaniak, A. Garton, D.J. Carlsson, D.M. Wiles, Examination of the crystal-structures present in Nylon-6 fibers, J. Polym. Sci. Pol. Phys. 17 (6) (1979) 987–999.

[34] Y. Liu, L. Cui, F. Guan, Y. Gao, N.E. Hedin, L. Zhu, H. Fong, Crystalline morphology and polymorphic phase transitions in electrospun Nylon-6 nanofibers, Macromolecules 40 (17) (2007) 6283–6290.
[35] F.L. Beyer, C. Ziegler, Wide-angle x-ray scattering characterization of the morphology of nylon 6 6 obturator materials, DTIC Doc. (2004) 1–15.
[36] J. Brisson, F. Brisse, Model compounds of aromatic nylons .2. Study of N,N'-Trimethylenebis(Para-Methoxybenzamide), N,N'-Pentamethylenebis(Para-Methylbenzamide), and N,N'-Heptamethylenebis(Para-Methylbenzamide) by x-ray-diffraction, Ir spectroscopy, and C-13 Cp/Mas nmr-spectroscopy, Macromolecules 22 (4) (1989) 1974–1981.
[37] R.S. Stein, A. Misra, Morphological studies on polybutylene terephthalate, J. Polym. Sci. Polym. Phys. Ed. 18 (2) (1980) 327–342.
[38] (a) G.B. McGaughey, M. Gagné, A.K. Rappé, π-stacking interactions: ALIVE and well in proteins, J. Biol. Chem. 273 (25) (1998) 15458–15463;
(b) C.R. Martinez, B.L. Iverson, Rethinking the term "pi-stacking", Chem. Sci. 3 (7) (2012) 2191–2201;
(c) C.A. Hunter, J.K.M. Sanders, The nature of.pi.-.pi. interactions, J. Am. Chem. Soc. 112 (14) (1990) 5525–5534.
[39] (a) H. Xu, A.K. Das, M. Horie, M.S. Shaik, A.M. Smith, Y. Luo, X. Lu, R. Collins, S.Y. Liem, A. Song, P.L.A. Popelier, M.L. Turner, P. Xiao, I.A. Kinloch, R.V. Ulijn, An investigation of the conductivity of peptide nanotube networks prepared by enzyme-triggered self-assembly, Nanoscale 2 (6) (2010) 960–966;
(b) S. Joshi, S. Grigorian, U. Pietsch, P. Pingel, A. Zen, D. Neher, U. Scherf, Thickness dependence of the crystalline structure and hole mobility in thin films of low molecular weight poly(3-hexylthiophene), Macromolecules 41 (18) (2008) 6800–6808.
[40] P.N. Pusey, in: T. Zemb, P. Lindner (Eds.), Neutrons, X-ray, and Light: Scattering Methods Applied to Soft Condensed Matter, 2002. North-Holland.
[41] P.J. Flory, Statistical Mechanics of Chain Molecules, J. Wiley & Sons, 1969.
[42] C. Chevigny, F. Dalmas, E. Di Cola, D. Gigmes, D. Bertin, F. Boue, J. Jestin, Polymer-grafted-nanoparticles nanocomposites: dispersion, grafted chain conformation, and rheological behavior, Macromolecules 44 (1) (2011) 122–133.
[43] I.W. Hamley, V. Castelletto, Small-angle scattering of block copolymers: in the melt, solution and crystal states, Prog. Polym. Sci. 29 (9) (2004) 909–948.
[44] S.E. Harton, S.K. Kumar, H.C. Yang, T. Koga, K. Hicks, E. Lee, J. Mijovic, M. Liu, R.S. Vallery, D.W. Gidley, Immobilized polymer layers on spherical nanoparticles, Macromolecules 43 (7) (2010) 3415–3421.
[45] M. Van Der Schuur, R.J. Gaymans, Segmented block copolymers based on poly (propylene oxide) and monodisperse polyamide-6, T segments, J. Polym. Sci. Part A Polym. Chem. 44 (16) (2006) 4769–4781.
[46] A. Louhichi, E. Tamborini, N. Ghofraniha, F. Caton, D. Roux, J. Oberdisse, L. Cipelletti, L. Ramos, Nucleation and growth of micellar polycrystals under time-dependent volume fraction conditions, Phys. Rev. E 87 (3) (2013) 032306.
[47] G.P. Baeza, A.C. Genix, C. Degrandcourt, L. Petitjean, J. Gummel, M. Couty, J. Oberdisse, Multiscale filler structure in simplified industrial nanocomposite silica/SBR systems studied by SAXS and TEM, Macromolecules 46 (1) (2013) 317–329.
[48] G.J. Vroege, D.M. Thies-Weesie, A.V. Petukhov, B.J. Lemaire, P. Davidson, Smectic liquid-crystalline order in suspensions of highly polydisperse goethite nanorods, Adv. Mater. 18 (19) (2006) 2565–2568.
[49] A. Banc, A.-C. Genix, C. Dupas, M. Sztucki, R. Schweins, M.-S. Appavou, J. Oberdisse, Origin of small-angle scattering from contrast-matched nanoparticles: a study of chain and filler structure in polymer nanocomposites, Macromolecules 48 (18) (2015) 6596–6605.
[50] G.P. Baeza, A.-C. Genix, N. Paupy-Peyronnet, C. Degrandcourt, M. Couty, Oberdisse, j., Revealing nanocomposite filler structures by swelling and small-angle X-ray scattering, Faraday Discuss. 186 (0) (2016) 295–309.
[51] R.M. Versteegen, R. Kleppinger, R.P. Sijbesma, E. Meijer, Properties and morphology of segmented copoly (ether urea) s with uniform hard segments, Macromolecules 39 (2) (2006) 772–783.
[52] B.D. Olsen, R.A. Segalman, Self-assembly of rod–coil block copolymers, Mater. Sci. Eng. R Rep. 62 (2) (2008) 37–66.
[53] X. Wang, G. Guerin, H. Wang, Y. Wang, I. Manners, M.A. Winnik, Cylindrical block copolymer micelles and co-micelles of controlled length and architecture, Science 317 (5838) (2007) 644–647.
[54] R.C. Dougherty, Temperature and pressure dependence of hydrogen bond strength: a perturbation molecular orbital approach, J. Chem. Phys. 109 (17) (1998) 7372–7378.
[55] D. Gauthier, P. Baillargeon, M. Drouin, Y.L. Dory, Self-assembly of cyclic peptides into nanotubes and then into highly anisotropic crystalline materials, Angew. Chem. Int. Ed. 40 (24) (2001) 4635–4638.